Zeolitic Imidazolate Frameworks

International Edition: DOI: 10.1002/anie.201809921
German Edition: DOI: 10.1002/ange.201809921

Controlling Dissolution and Transformation of Zeolitic Imidazolate Frameworks by using Electron-Beam-Induced Amorphization

*Sabrina Conrad, Prashant Kumar, Feng Xue, Limin Ren, Sheryl Henning, Chunhong Xiao, K. Andre Mkhoyan, and Michael Tsapatsis**

Abstract: *Amorphous zeolitic imidazolate frameworks (ZIFs) offer promising applications as novel functional materials. Herein, amorphization of ZIF-L through scanning-electron-beam exposure is demonstrated, based on amorphization of individual ZIF-L crystals. The amorphized ZIF product has drastically increased stability against dissolution in water. An electron dose that allows for complete preservation of amorphous particles after immersion in water is established, resulting in new shapes of amorphous ZIF-L with spatial control at the sub-micrometer length scale. Changed water stability as a consequence of scanning-electron-beam exposure is demonstrated for three additional metal–organic frameworks (ZIF-8, Zn(BeIm)OAc, MIL-101), highlighting the potential use of an electron beam for top-down MOF patterning. Lastly, recrystallization of ZIF-L in the presence of linker is studied and shows distinct differences for crystalline and amorphized material.*

Zeolitic imidazolate frameworks (ZIFs) are metal–organic frameworks (MOFs) with topologies analogous to those known for zeolites.[1] Efforts to tailor the pore structure and functional properties of ZIFs for uses in gas storage, gas separation, and catalysis have resulted in the development of numerous novel ZIF topologies and compositions.[1,2] At the same time, post-synthetic functionalization and processing techniques have been explored to arrive at modified ZIF materials that are derived from existing frameworks.[3] Along with crystalline ZIFs, amorphous ZIFs have been obtained from their crystalline counterparts through heating,[4] pressurizing,[5] ball-milling,[6] and electrical discharge[7] procedures, and explored for applications, such as guest immobilization and drug delivery.[6a,8] Amorphous ZIFs, owing to their distinct yet closely related structure to the parent ZIF, may also provide a platform to complement thin-film deposition and patterning techniques, which are currently being developed for ZIF integration in thin-film membranes, sensors, and low-k dielectric devices.[4,5a,9,10] Herein, we demonstrate that a scanning electron beam can be used for immediate amorphization of a layered ZIF (known as ZIF-L),[11] resulting in an amorphized product with retained short-range structure but lack of long-range order. Amorphous ZIF-L exhibits remarkable differences in dissolution rates in water and distinct (single vs. polycrystal) behavior in linker-vapor induced crystallization to ZIF-8. Although it is not possible to assess the reasons for this behavior, targeted experimental approaches will help to further elucidate the underlying mechanisms in the future.

ZIF-L crystals with 2-dimensional leaf-like morphology (size: ca. 2 μm × 6 μm, thickness: 100–200 nm) were prepared in aqueous media from Zn nitrate and 2-methylimidazole according to a reported procedure (for details on the synthesis of ZIF-L see Experimental Methods in the Supporting Information).[11] Fresh crystals were deposited on carbon-coated copper transmission electron microscope (TEM) grids. Exposure of ZIF-L crystals to the beam of a scanning electron microscope (SEM) for amorphization was performed in a JEOL 6700 and JEOL 6500 SEM equipped with field emission guns operating at 5 kV. A low-magnification image was recorded first to locate a marked deposit area, prior to scanning individual crystals at high magnification. The applied electron doses under low and high magnification conditions were determined as 2.7×10^{-6} and 1.1×10^{-2} C cm^{-2}, respectively (Table S1 in the Supporting Information). The penetration depth of the e-beam in ZIF-L for an acceleration voltage of 5 kV was calculated with the Monte Carlo simulation program CASINO (http://www.gel.usherbrooke.ca/casino/What.html), and found to be approximately 450 nm, which exceeds the average ZIF-L particle thickness. Following exposure in the SEM, tracking of the same region of deposit with TEM was used to probe the crystallinity of individual ZIF-L particles, employing low-dose imaging conditions. Control experiments confirmed that scanning electron beam exposure at low magnification, and imaging/diffraction in the TEM at a minimal dose have no adverse effects on the crystallinity of ZIF-L (Figure S1 and S2 a,b).

First, ZIF-L crystals with no prior scanning electron beam exposure were investigated. A representative electron diffraction (ED) pattern and corresponding TEM image are displayed in Figure 1 b. The thin dimension of the leaf-shaped crystals is determined to be along the *a*-axis (Figure 1 a; Figure S3).

It was then attempted to record ED patterns of ZIF-L particles previously imaged at high magnification in an SEM (Figure 1 d). In this case, lack of sharp diffraction spots was evident, indicating loss of crystallinity during scanning

[*] Dr. S. Conrad, P. Kumar, F. Xue, Dr. L. Ren, Prof. K. A. Mkhoyan, Prof. M. Tsapatsis
Department of Chemical Engineering and Materials Science
University of Minnesota
Washington Ave SE, Minneapolis, MN 55455 (USA)
E-mail: tsapatsis@umn.edu
S. Henning, C. Xiao
Thermo Fisher Scientific
5225 Verona Road, Madison, WI 53711 (USA)
Supporting information and the ORCID identification number(s) for the author(s) of this article can be found under: https://doi.org/10.1002/anie.201809921.

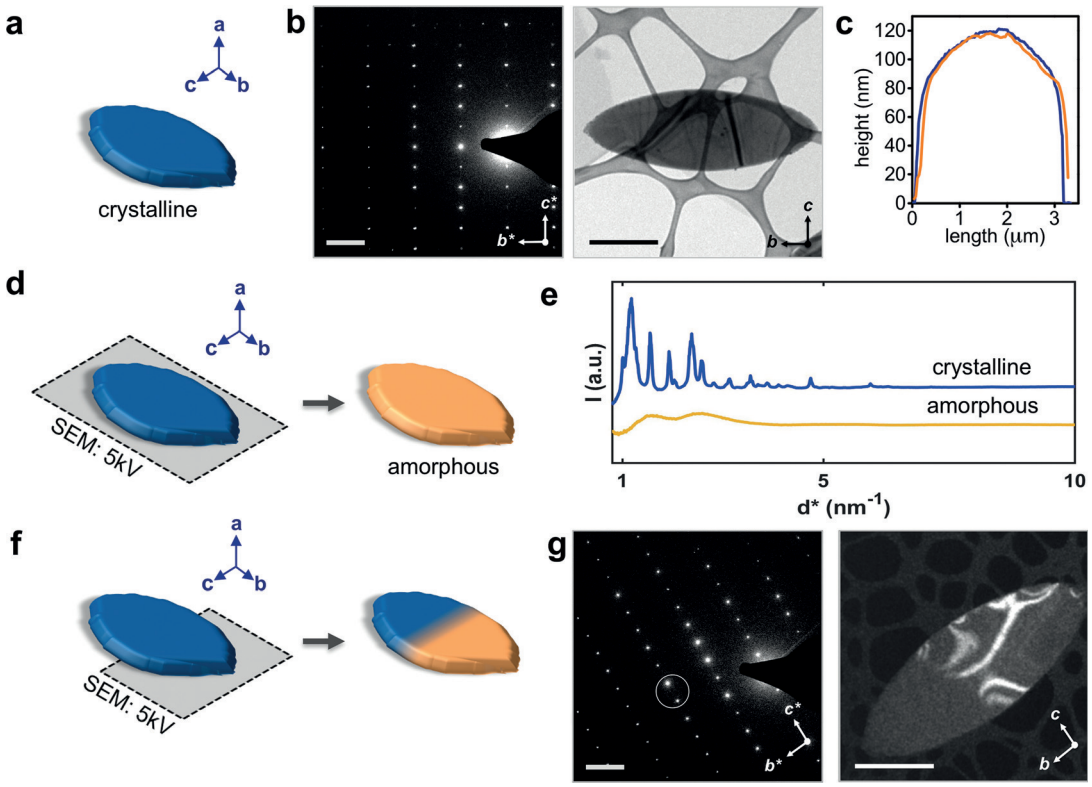

Figure 1. a) Schematic representation of a crystalline ZIF-L particle. b) [100] zone axis ED pattern (left) and bright-field TEM image (right) of a ZIF-L particle. c) AFM height profiles for a ZIF-L particle along the *b*-axis, before (blue) and after (orange) high-magnification SEM imaging. d) Schematic of the exposure of ZIF-L to an SEM beam. e) Line scans from radially averaged ED patterns of a crystalline ZIF-L particle (blue) and a ZIF-L particle after SEM exposure as depicted in (d) (orange), as intensity in arbitrary units. f) Schematic representation of the partial exposure of a ZIF-L particle to a high-magnification SEM beam. g) [100] zone axis ED pattern (left) and dark-field TEM image (right) of a ZIF-L particle after partial exposure as depicted in (f). Scale bars in (b) are 1 nm^{-1} and 1 μm; in (g) 1 nm^{-1} and 1 μm.

electron beam exposure (Figure S2c). Examination of several crystals at this stage did not yield sharp diffraction spots, indicating that high magnification SEM imaging (electron dose: 1.1×10^{-2} C cm^{-2}; acceleration voltage: 5 kV) caused amorphization of ZIF-L. (Further analysis below will discuss the presence of diffuse scattering.)

To demonstrate selective amorphization within a single particle, we reduced the area imaged at high magnification to about half of a ZIF-L crystal (Figure 1f). After exposure, an identical diffraction pattern to that of pristine ZIF-L was obtained from the entire particle (Figure 1g, left). However, dark-field TEM images (Figure 1g, right) revealed that the portion of ZIF-L exposed to high magnification SEM imaging was amorphous appearing dark in dark-field mode, while the other half was crystalline exhibiting bright stripes.

The observed bright stripes in the TEM dark-field image (Figure 1g, right) are bend contours, which occur as a result of out-of-plane ZIF-L crystal surface curvature, leading to diffracting planes that are not everywhere parallel to the beam.[12] Such curvature is evident in the atomic force microscopy (AFM) height profile shown in Figure 1c (see blue trace for crystalline ZIF-L). Analogous dark stripes can be observed in TEM bright-field images of ZIF-L (Figure 1b, right, and Figure S4).

Amorphization of ZIFs has been associated with highly disordered framework structures retaining the basic metal-ligand connectivity while lacking long-range order.[8b] E-beam amorphization of ZIF-L takes place without dimensional changes or the build-up of nanoparticulate degradation products as shown by AFM (Figure 1c) and high-angle annular dark-field scanning transmission electron microscopy (Figure S5). This suggests that SEM beam exposure of ZIF-L triggers similar internal rearrangements without decomposition of the linker, resulting in amorphous ZIF-L with intact short-range structure.

To obtain further insight into the disordered nature of amorphized ZIF-L, the structure of crystalline and amorphous ZIF-L was compared using a radial distribution analysis of ED data. While crystalline ZIF-L yielded sharp diffraction spots, diffuse scattering was obtained for amorphous ZIF-L with two broad features centered at d-spacings of 6.26 (1.597 nm^{-1}) and 3.89 Å (2.569 nm^{-1}; Figure 1e and Figure S2d). These peaks were different from the diffuse scattering peaks arising from the amorphous carbon support. The ratios of these d-spacing values (1.6) coincide with allowed reflections for a body-centered-cubic (BCC) lattice ($d_{110}/d_{200} = 1.4$ & $d_{110}/d_{211} = 1.7$), implying that the structure of amorphous ZIF-L is consistent with a BCC unit cell. Considering the structural similarity between ZIF-L and its cubic polymorph ZIF-8, it is conceivable that ZIF-L amorphization entails the formation of an amorphous version of ZIF-8.

Although an earlier study demonstrated lengthened release times for encapsulated drug molecules in the mechanically amorphized MOF UiO-66 compared to its crystalline precursor,[8a] no studies exist thus far to demonstrate amorphization-induced stabilization of MOFs to dissolution. Therefore, the impact of e-beam amorphization on the water resistance of ZIF-L was assessed. For these studies, a deposit of ZIF-L was formed on marked silicon wafers by placing the wafers horizontally in freshly prepared crystal suspensions to allow crystals to settle and deposit with their flat surface parallel to the wafer surface. Then, a ZIF-L crystal or crystal region was amorphized by recording an SEM image of a specified region at high magnification. Figure 2a shows tilted-view AFM three-dimensional height images of a half-amorphized ZIF-L particle before and after immersion in deionized water for 1 h (for details on the water stability tests see Experimental Methods in Supporting Information). Complete degradation of the crystalline region of the particle was evident (right portion in this view) while the amorphous region was preserved, which is also evident from corresponding AFM height profiles (Figure 2c, top). Consistently, the same experiment with crystalline ZIF-L revealed complete dissolution of the ZIF crystal (Figure 2b,c, Figure S6), whereas amorphous ZIF-L remained intact without detectable changes in shape or size.

These observations indicate that amorphized ZIF-L possesses drastically increased water stability compared to its crystalline parent framework. X-ray photoelectron spectroscopy (XPS) analysis of water-resistant ZIF-L ruled out major changes in the surface region compared to crystalline ZIF-L (Figure S7), affirming that the increase in stability is not an effect of changes in surface composition occurring during water exposure. Additionally, IR analysis of crystalline and water-resistant ZIF-L showed close similarity between spectra of the two materials. Specifically, the fingerprint region of both spectra show vibrations that have previously been assigned to imidazolate units and Zn–N bonds of ZIF-L (see Figure S8 and Ref. [13]), confirming that linker molecules and linker-to-metal bonds stay intact during e-beam-induced amorphization. Moreover, a peak that has previously been ascribed to the C=N stretch of ZIF-8 (1584 cm^{-1})[13] is more pronounced in SEM amorphized ZIF-L compared to crystalline ZIF-L (see Figure S8). This observation further supports our hypothesis that the structure of SEM-amorphized ZIF-L is consistent with that of amorphous ZIF-8. Similarly, a ring stretch that appears in the spectrum of crystalline ZIF-L (1100 cm^{-1}) is absent in the spectrum of ZIF-8 and amorphized ZIF-L.

The above results demonstrate that e-beam exposure can be used for ZIF-L amorphization resulting in a disordered cubic structure with remaining short-range order, which exhibits enhanced stability against dissolution in water. Considering the well-established e-beam sensitivity of ZIFs, it is not surprising that long-range order may be lost, as there are various elastic and inelastic electron-MOF scattering mechanisms that can adversely affect specimens during e-beam imaging, including temperature rise, electrical discharge and ionization.[14] In organic materials, such as ZIFs, ionization damage is of prime importance, implying distortion and disruption of chemical bonds as a result of inelastic scattering of primary and secondary electrons.[14a,b] These processes, which can lead to the release of hydrogen atoms and the creation of radicals,[15] cause structural disorder and can alter the chemical nature of a material. For SEM-imaged ZIF-L, structural disorder became evident as lack of sharp diffraction spots in its ED pattern (Figure 1 and Figure S2c). However, our XPS and IR analysis ruled out drastic chemical changes to the ZIF framework. Based on these findings, the observed stabilization is likely a consequence of local structural rearrangements[8b] that make hydrolysable metal nodes less accessible, causing prolonged degradation pathways in aqueous media. Over-coordination of the zinc centers with imidazolate-ligands (ligand/Zn > 4) might contribute to this stabilization,[16] since the transformation from ZIF-L to ZIF-8 is accompanied by release of ligands that remain in the ZIF framework after SEM amorphization. Additionally, it is possible that a very thin protective coating of unknown structure is created on the surface of ZIF-L from e-beam-induced carbon contamination, protecting it from dissolution.[14a] Although this possibility cannot be fully excluded and should be the subject of future studies, ZIF-L particles that were coated with carbon in an ion-beam sputtering system prior to immersion in water did not show enhanced resistance to dissolution.

The ability to selectively dissolve the original ZIF-L crystal leaving the amorphized part intact

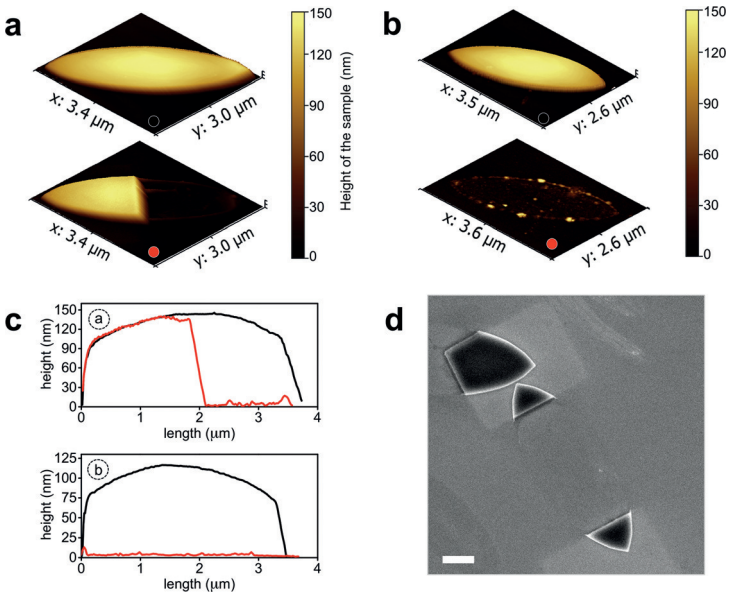

Figure 2. a) AFM height images of a partially exposed ZIF-L particle before (top) and after (bottom) immersion in deionized water. b) AFM height images of a ZIF-L particle without prior SEM exposure before (top) and after (bottom) immersion in deionized water. c) AFM height profiles of the height images shown in (a) and (b) (along the *b*-axis, black before immersion, red after immersion). d) SEM image of partially exposed ZIF-L particles after immersion in deionized water. Scale bar in (d) is 1 µm.

opens exciting opportunities for e-beam patterning of ZIF/MOF materials. To further illustrate the potential for microscale control, Figure 2d shows an SEM image of two partially amorphized ZIF-L particles resulting in newly shaped amorphous ZIF-L deposits after dissolving the crystalline regions.

Dissolution sequences were then recorded for various electron doses applied to ZIF-L to establish a critical electron dose value $D_{e,c}$ that achieves complete preservation of exposed crystals. Electron dosage was adjusted by altering the magnified area while keeping probe current and exposure time unchanged. As before, complete dissolution of the crystalline regions of the particles was evident, whereas the exposed regions showed decreasing resistance to dissolution going from high to low electron doses (Figure S9a). Interestingly, these sequences reveal that the level of e-beam exposure and duration of the subsequent dissolution provide an opportunity to control the thickness of the remaining ZIF-L (Figure S9a). Quantitative analysis of several AFM height profiles before and after immersion in water yielded a critical electron dose $D_{e,c}$ of approximately $1.2 \times 10^{-2}\,C\,cm^{-2}$ (Figure S9b–d), representing a threshold value to obtain water-resistant amorphized ZIF-L by scanning electron beam exposure.

Next, we investigated if similar phenomena can be observed for other ZIFs/MOFs. ED analysis of nanoparticulate ZIF-8 revealed that high-magnification SEM imaging induces loss of crystallinity, as observed for ZIF-L (Figure S10c; for details on the synthesis of ZIF-8 see Experimental Methods in the Supporting Information). The contribution of ZIF-8 to the rotational pattern is smaller compared to ZIF-L since less sample is included in the diffraction aperture, resulting in indistinguishable diffuse scattering for amorphous ZIF-8 and the TEM support (Figure S10d). To establish if ZIF-8 amorphization entails a change in water stability, as observed for ZIF-L, similar dissolution studies were performed for ZIF-8. As before, SEM beam exposure included one low and one high magnification image (Figure 3a), resulting in two SEM images (Figure 3c, (1) and (2)). The same sample area was examined with SEM after immersion in water (Figure 3d, (1) and (2)). The small region of ZIF-8 deposit was fully retained (2), though all particles around it were dissolved ((1) minus (2)), suggesting that ZIF-8 amorphization leads to enhanced water stability of ZIF-8. ZIF-8 particles located at the transition between low- and high-magnified regions revealed partial dissolution (Figure 3b), confirming that the disappearance of ZIF-8 deposit is a result of material dissolution, rather than release of intact particles from the wafer surface. Variation of the applied electron dose revealed gradual changes to the water resistance of ZIF-8 (Figure S11), emphasizing a similar impact of SEM beam exposure on the water stability of ZIF-8 and ZIF-L.

Dissolution studies were then performed for Zn(BeIm)OAc nanosheets and nanoparticulate MIL-101 to elucidate if our findings are applicable to different MOF frameworks (for details on the synthesis of Zn(BeIm)OAc and MIL-101 see Experimental Methods in the Supporting Information). Similar results arising for these frameworks indicate that scanning electron beam exposure at high magnification stabilizes Zn(BeIm)OAc and MIL-101 against dissolution in water (Figure S12 and S13).

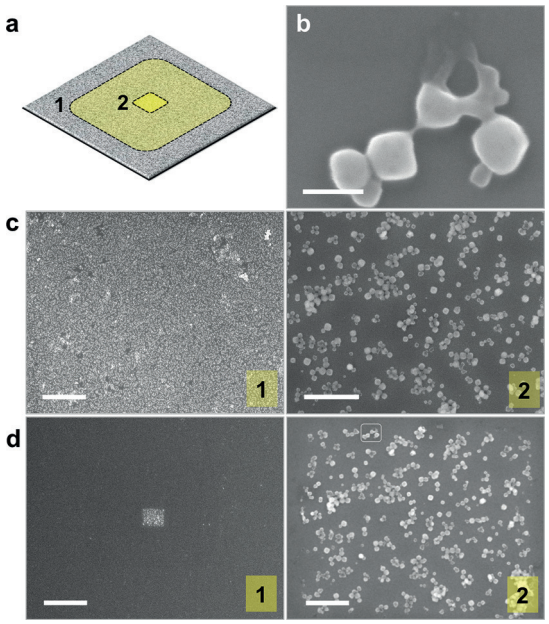

Figure 3. a) Schematic representation of ZIF-8 SEM exposure. b) Magnification of ZIF-8 particles at the boundary of area (1) and (2). c) Low- and high-magnification SEM image of ZIF-8 deposit of (1) and (2). d) SEM images of the sample areas shown in (c) after immersion in deionized water. The scale bar in (b) is 100 nm. The scale bars from left to right in (c) and (d) are 10 μm and 1 μm.

The above findings could be of interest for emerging efforts towards top-down MOF patterning techniques, which are still in their infancy but attractive due to available MOF synthesis protocols.[10,17] Patterning methods allow controlled positioning of specimen in the lateral space, which is crucial for their use in sensing and microelectronic devices.[10] Our work implies that such control could be achieved by making use of the selective preservation of amorphized MOF during solvent processing (Figure 2d). Where applicable, this approach could produce amorphous nanostructures by using high-resolution electron-beam lithography for amorphization.

In addition to displaying crystal-to-amorphous transformations, MOFs are inherently inclined to undergo crystal-to-crystal-transformations under various external stimuli.[13,18] Similarly, MOF-based amorphous-to-crystalline transformations have been described, some of which allow for reversible modulation between amorphous and crystalline counterpart.[5b] In light of this, we investigated the phase transformation of crystalline and amorphous ZIF-L to assess how disrupted long-range order impacts the microstructure of the resulting phase. A linker-vapor infused atmosphere, known to enable ZIF growth by contact with a Zn source,[9a] was selected in an attempt to favor recrystallization of amorphous ZIF-L. Experiments were performed by exposure of ZIF-L deposit to MeIm vapor at 100 °C according to a reported procedure that converts ZnO to ZIF-8.[9a]

First, the behavior of crystalline ZIF-L was assessed. After MeIm vapor-exposure, morphological changes were

evident in bright-field (BF) TEM images and AFM height profiles (Figure 4a and Figure S14a; c.f. Figure 1b). Micrometer-sized crystals with well-defined facets had evolved and were grouped in a ring-shaped ensemble corresponding to the

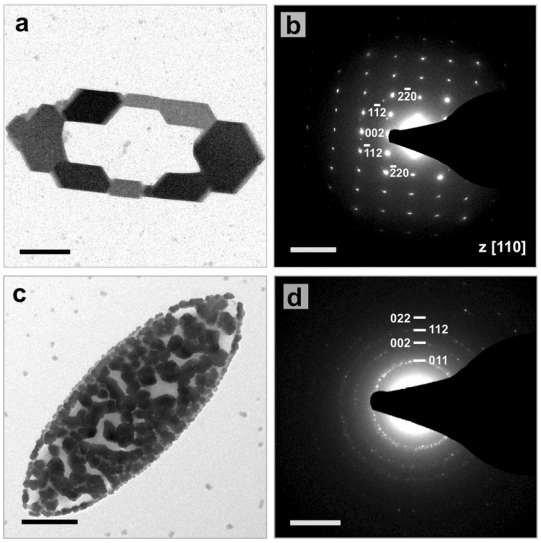

Figure 4. a) BF-TEM image of single-crystal-like ZIF-8 formed by linker vapor treatment of ZIF-L. b) [110] zone axis ED pattern of the entire ZIF-8 particle in (a). c) BF-TEM image of polycrystalline ZIF-8 crystals formed by linker vapor treatment of amorphous ZIF-L. d) ED pattern of polycrystalline ZIF-8 in (c). Scale bars in (a) and (b) are 0.5 μm and 2 nm^{-1}; in (c) and (d) 1 μm and 1 nm^{-1}.

contour of the parent ZIF-L, suggesting internal rearrangements that consume the central part of ZIF-L while building up crystalline framework at the periphery. Examination of the entire ensemble of emerged crystals with electron diffraction revealed the formation of monocrystalline ZIF-8 exposing its (110) facet (Figure 4b), which confirmed that ZIF-L underwent topotactic transformation to crystallographically aligned ZIF-8 crystals (nearly single-crystal-like). A similar treatment was then performed for electron-beam amorphized ZIF-L. TEM images and AFM height profiles showed formation of nano- and micrometer-sized round-shaped particles (Figure 4c and S14b). Electron diffraction (Figure 4d) showed a well-defined ring pattern consistent with polycrystalline ZIF-8, indicating that exposure of amorphous ZIF-L to linker vapor entails a different phase transformation behavior than it was detected for crystalline ZIF-L.

The scanning-electron-beam-induced amorphization of ZIF-L described here allows for unprecedented control in the fabrication of amorphous ZIF-L features. It appears to be applicable to other MOFs (ZIF-8, Zn(BeIm)OAc, MIL-101) and is expected to enable ZIF and MOF film patterning. Furthermore, the ability to perturb long-range connectivity in individual ZIF crystals gave access to new findings on dissolution and phase transformation behavior of crystalline versus amorphous ZIFs with implications towards understanding ZIF and MOF stability and crystallization.

Acknowledgements

This work was supported by the Center for Gas Separations Relevant to Clean Energy Technologies, an Energy Frontier Research Center funded by the US Department of Energy, Office of Science, Basic Energy Sciences under Award DE-SC0001015. Parts of this work were carried out in the Characterization Facility, University of Minnesota, which receives partial support from the National Science Foundation through the MRSEC program. Portions of this work were conducted in the Minnesota Nano Center, which is supported by the National Science Foundation through the National Nano Coordinated Infrastructure Network (NNCI) under Award Number ECCS-1542202.

Conflict of interest

The authors declare no conflict of interest.

Keywords: amorphous materials · metal–organic frameworks (MOFs) · patterning · scanning probe techniques · ZIF-L

How to cite: *Angew. Chem. Int. Ed.* **2018**, *57*, 13592–13597
Angew. Chem. **2018**, *130*, 13780–13785

[1] A. Phan, C. J. Doonan, F. J. Uribe-Romo, C. B. Knobler, M. O'Keeffe, O. M. Yaghi, *Acc. Chem. Res.* **2010**, *43*, 58–67.
[2] a) B. Chen, Z. Yang, Y. Zhu, Y. Xia, *J. Mater. Chem. A* **2014**, *2*, 16811–16831; b) K. S. Park, Z. Ni, A. P. Côté, J. Y. Choi, R. Huang, F. J. Uribe-Romo, H. K. Chae, M. O'Keeffe, O. M. Yaghi, *Proc. Natl. Acad. Sci. USA* **2006**, *103*, 10186–10191; c) Y.-Q. Tian, C.-X. Cai, X.-M. Ren, C.-Y. Duan, Y. Xu, S. Gao, X.-Z. You, *Chem. Eur. J.* **2003**, *9*, 5673–5685.
[3] a) W. Morris, C. J. Donnan, H. Furukawa, R. Banerjee, O. M. Yaghi, *J. Am. Chem. Soc.* **2008**, *130*, 12626–12627; b) A. Huang, J. Caro, *Angew. Chem. Int. Ed.* **2011**, *50*, 4979–4982; *Angew. Chem.* **2011**, *123*, 5083–5086.
[4] a) T. D. Bennett, A. L. Goodwin, M. T. Dove, D. A. Keen, M. G. Tucker, E. R. Barney, A. K. Soper, E. G. Bithell, J.-C. Tan, A. K. Cheetham, *Phys. Rev. Lett.* **2010**, *104*, 115503; b) T. D. Bennett, D. A. Keen, J.-C- Tan, E. R. Barney, A. L. Goodwin, A. K. Cheetham, *Angew. Chem. Int. Ed.* **2011**, *50*, 3067–3071; *Angew. Chem.* **2011**, *123*, 3123–3127.
[5] a) K. W. Chapman, G. J. Halder, P. J. Chupas, *J. Am. Chem. Soc.* **2009**, *131*, 17546–17547; b) T. D. Bennett, P. Simoncic, S. A. Moggach, F. Gozzo, P. Machi, D. A. Keen, J.-C. Tan, A. K. Cheetham, *Chem. Commun.* **2011**, *47*, 7983–7985.
[6] a) T. D. Bennett, S. Cao, J.-C- Tan, D. A. Keen, E. G. Bithell, P. J. Beldon, T. Friscic, A. K. Cheetham, *J. Am. Chem. Soc.* **2011**, *133*, 14546–14549; b) T. D. Bennett, P. J. Saines, D. A. Keen, J.-C. Tan, A. K. Cheetham, *Chem. Eur. J.* **2013**, *19*, 7049–7055.
[7] Y. Zhou, C.-J. Liu, *Plasma Chem. Plasma Process.* **2011**, *31*, 499–506.
[8] a) C. Orellana-Tavra, E. F. Baxter, T. Tian, T. D. Bennett, N. K. H. Slater, A. K. Cheetham, D. Fairen-Jiminez, *Chem. Commun.* **2015**, *51*, 13878–13881; b) T. D. Bennett, A. K. Cheetham, *Acc. Chem. Res.* **2014**, *47*, 1555–1562.
[9] a) I. Stassen, M. Styles, G. Grenci, H. V. Gorp, W. Vanderlinden, S. De Feyter, P. Falcaro, D. De Vos, P. Vereecken, R. Ameloot, *Nat. Mater.* **2016**, *15*, 304–310; b) H. T. Kwon, H.-K. Jeong, A. S. Lee, H. S. An, J. S. Lee, *J. Am. Chem. Soc.* **2015**, *137*, 12304–

12311; c) J.-R. Li, R. J. Kuppler, H.-C. Zhou, *Chem. Soc. Rev.* **2009**, *38*, 1477 – 1504.
[10] a) P. Falcaro, R. Ricco, C. M. Doherty, K. Liang, A. J. Hill, M. J. Styles, *Chem. Soc. Rev.* **2014**, *43*, 5513 – 5560; b) I. Stassen, N. Burtch, A. Talin, P. Falcaro, M. Allendorf, R. Ameloot, *Chem. Soc. Rev.* **2017**, *46*, 3185 – 3241.
[11] R. Chen, J. Yao, Q. Gu, S. Smeets, C. Baerlocher, H. Gu, D. Zhu, W. Morris, O. M. Yaghi, H. Wang, *Chem. Commun.* **2013**, *49*, 9500 – 9502.
[12] D. B. Williams, C. B. Carter, *Transmission Electron Microscopy Part 1: Basics*, Springer, New York, **2009**, pp. 411 – 412.
[13] Z.-X. Low, J. Yao, Q. Liu, M. He, Z. Wang, A. K. Suresh, J. Bellare, H. Wang, *Cryst. Growth Des.* **2014**, *14*, 6589 – 6598.
[14] a) R. F. Egerton, P. Li, M. Malac, *Micron* **2004**, *35*, 399 – 409; b) R. F. Egerton, *Ultramicroscopy* **2013**, *127*, 100 – 108; c) H. Greer, W. Zhou, *Crystallogr. Rev.* **2011**, *17*, 163 – 185; d) C. Wiktor, M. Meledina, S. Turner, O. I. Lebedev, R. A. Fischer, *J. Mater. Chem. A* **2017**, *5*, 14969 – 14989.
[15] A. Ribar, K. Fink, Z. Li, S. Ptasinska, I. Carmicahel, L. Feketeova, S. Denifl, *Phys. Chem. Chem. Phys.* **2017**, *19*, 6406 – 6415.
[16] T. Dudev, C. Lin, *J. Am. Chem. Soc.* **2000**, *122*, 11146 – 11153.
[17] C. Dimitrakakis, B. Marmiroli, H. Amenitsch, L. Malfatti, P. Innocenzi, G. Grenci, L. Vaccari, A. J. Hill, B. P. Ladewig, M. R. Hill, P. Falcaro, *Chem. Commun.* **2012**, *48*, 7483 – 7485.
[18] J. Zhang, T. Zhang, D. Yu, K. Xiao, Y. Hong, *CrystEngComm* **2015**, *17*, 8212 – 8215.

Manuscript received: August 28, 2018
Accepted manuscript online: August 31, 2018
Version of record online: August 31, 2018

